

# <sup>1</sup> Pore-pressure diffusion controls upper-plate <sup>2</sup> aftershocks of the 2014 Iquique earthquake

<sup>3</sup> Carlos Peña<sup>1,2\*</sup>, Oliver Heidbach<sup>1,3</sup>, Sabrina Metzger<sup>1</sup>, Bernd Schurr<sup>1</sup>, Marcos Moreno<sup>4</sup>,  
<sup>4</sup> Onno Oncken<sup>1,5</sup>, and Claudio Faccenna<sup>1,6</sup>

<sup>5</sup> <sup>1</sup>Helmholtz GFZ German Research Centre for Geosciences, Potsdam, Germany

<sup>6</sup> <sup>2</sup>Institute of Geosciences, University of Potsdam, Potsdam, Germany

<sup>7</sup> <sup>3</sup>Technical University of Berlin, Berlin, Germany

<sup>8</sup> <sup>4</sup>Department of Geophysics, University of Concepción, Concepción, Chile

<sup>9</sup> <sup>5</sup>Department of Earth Sciences, Free University Berlin, Berlin, Germany

<sup>10</sup> <sup>6</sup>Dipartimento di Scienze, Università Roma Tre, Rome, Italy

<sup>11</sup> \*carlosp@gfz-potsdam.de

## <sup>12</sup> ABSTRACT

Upper-plate aftershocks following megathrust earthquakes are particularly dangerous as they may occur close to the highly populated shore. Aftershock numbers decay with time, imposing a time-dependent seismic hazard. While coseismic stress transfer cannot explain this time-dependency, transient postseismic deformation due to afterslip, viscoelastic relaxation, and pore-pressure diffusion are potential candidates. We investigate which of these three processes is the key driver of the upper-plate aftershocks following the 2014 Mw=8.1 Iquique, northern Chile, earthquake. We first use a 4D (space and time) model to reproduce the postseismic deformation observed in geodetic data. We <sup>13</sup> then analyze the spatiotemporal stress changes produced by individual postseismic processes and compare them to the distribution of upper-plate aftershocks. Our results reveal that stresses produced by coseismically-induced pore-pressure diffusion best correlate in space and time with increased upper-plate aftershock activity. Moreover, an increase in pore-pressure diffusion reduces the three principal stresses likewise. Hence, all faults, regardless of their orientation, are brought closer to failure. This may explain the diversity of faulting styles of upper-plate aftershocks. Our findings provide new insights into the link between pore-pressure diffusion and upper-plate deformation in subduction zones with implications for time-dependent seismic hazard assessment.

<sup>14</sup> Keywords: Pore pressure, upper-plate aftershocks, subduction

## <sup>15</sup> Main

### <sup>16</sup> Mechanisms of upper-plate aftershocks

<sup>17</sup> Aftershocks are a global time-dependent process in the aftermath of large earthquakes, as first observed by  
<sup>18</sup> Omori<sup>1</sup> in 1894. At subduction zones, upper-plate aftershocks are particularly important since they pose a  
<sup>19</sup> higher seismic risk due to their relatively shallow depth. Aftershock numbers exhibit an exponential decay

over time<sup>2</sup>. They occur delayed from the main shock by days to weeks, such as the Pichilemu ( $M_w=7.0$  and  $M_w=6.9$ ) events 12 days after the 2010  $M_w$  8.8 Maule (Chile) earthquake, or even later, after several months or years<sup>2–4</sup>. Unlike the aftershocks along the megathrust itself, the events in the upper plate can show variable faulting styles (e.g., thrust, normal, or strike-slip) types as observed following the 2011 Tohoku-Oki (Japan), 2010 Maule and 2014 Iquique (Chile), 2004 Sumatra-Andaman (Indonesia), and 2015 Gorkha (Nepal) megathrust events<sup>3–6</sup>. Upper-plate aftershocks have been widely investigated by static or dynamic coseismic stress changes<sup>2,3,7–10</sup> mainly using the parameter Coulomb Failure Stress changes ( $\Delta CFS$ , see methods). Here, positive  $\Delta CFS$  values indicate that the stress state has been brought closer to failure, while negative  $\Delta CFS$  values further away from failure<sup>7</sup>. However, even when coseismic  $\Delta CFS$  may explain the spatial distribution of some events<sup>2,3,8</sup>, they fail to explain the time dependency. A plausible candidate to explain the time dependency may be the postseismic crustal deformation exhibiting similar exponential time decay. Despite the significant scientific efforts<sup>11,12</sup>, it remains unclear which postseismic deformation process dominates stress changes that drive the aftershock sequence in the upper plate.

#### 34 Key drives of postseismic deformation

Postseismic deformation is controlled by aseismic slip (afterslip) along the fault interface, non-linear viscoelastic stress relaxation in the lower crust and upper mantle, and pore-pressure diffusion in the upper plate induced by the main shock<sup>11,13–17</sup>. These deformation processes act at different spatiotemporal scales. Afterslip and pore-pressure diffusion dominate the near-field deformation, i.e., close to the region of most significant coseismic slip release, and may last up to several years<sup>11,18</sup>. On the other hand, non-linear viscoelastic relaxation controls the far-field deformation by up to several decades, albeit it may also contribute to the near-field deformation during the first months of the postseismic phase<sup>11</sup>. Indeed, pore-pressure changes have been proposed to control the occurrence of aftershocks quite a while ago in 1972, given their controlling effect on the effective normal fault stress<sup>19</sup>. This has been extensively studied during subsurface fluid operations in geothermal systems or waste-water disposal at depth<sup>20–22</sup>, as well as in natural hydrothermal or over-pressured fluid systems in normal faulting and strike-slip regimes<sup>23–25</sup>. Although still debated at subduction zones, the presence of higher pore-fluid pressure in the fault zone and upper plate due to metamorphic dehydration reactions from the oceanic plate<sup>26,27</sup> suggest that pore-pressure diffusion may play a role in the generation of upper-plate aftershock activity and/or other seismological processes. For instance, transient changes of seismic velocity ( $v_p/v_s$  ratio) in the upper plate<sup>28,29</sup>, the spatiotemporal migration front imaged by aftershocks<sup>30–32</sup>, and some shallow crustal aftershocks<sup>11</sup> have been associated with pore-pressure diffusion induced by the main shock in the Chilean, Northern Japan, and Indonesian subduction regions. Nevertheless, a direct link between the occurrence of upper-plate aftershocks in space and time with pore-pressure diffusion remains to be demonstrated. Here, we use comprehensive seismological and geodetic datasets in northern Chile to investigate with a 4D hydro-mechanical-numerical model which stress changing process is the key driver of the upper-plate aftershocks following the  $M_w=8.1$  Iquique megathrust earthquake.

57 **Modelling the Iquique megathrust earthquake deformation and stress changes**

58 The Iquique earthquake occurred on April 1st, 2014, in northern Chile<sup>33</sup> (inset in Fig. 1). The deformation  
59 before, during, and after the Iquique earthquake has been continuously monitored for more than 15 years  
60 with a high spatial and temporal resolution by state-of-the-art geodetical and geophysical instrumentation  
61 within the Integrated Plate Boundary Observatory Chile (IPOC) network<sup>33–35</sup>. In particular, the seismic  
62 and geodetic network detected significant non-linear, transient surface deformation and numerous upper-  
63 plate aftershocks showing a diversity of faulting styles following the main shock<sup>5,34,36</sup> (Fig. 1, Fig.  
64 2). These observations allow examining the hypothesis that the increase in upper-plate seismicity in  
65 space and time following the main shock is controlled by the distribution of pore-pressure diffusion. To  
66 investigate this, we combine a new 4D forward and geodetic inversion model for northern Chile, Global  
67 Navigation Satellite System (GNSS) measurements, seismicity, and focal mechanisms catalogs. We invert  
68 for the afterslip distribution using the GNSS data considering the effects of poroelasticity and non-linear  
69 viscoelasticity<sup>11</sup>. Our model can accurately explain the observed geodetic surface displacement patterns in  
70 space and time, which are usually overlooked in aftershocks studies in general<sup>9,10,25,28,30,31</sup>. To visualize  
71 the results of the spatiotemporal stress change, we use the parameter  $\Delta CFS$  for each of the individual  
72 postseismic processes and compare these with a seismicity catalog<sup>36</sup> and earthquake focal mechanisms<sup>5</sup>.  
73 We finally show that the increased number and patterns of upper-plate aftershocks are unambiguously  
74 better explained by pore-pressure diffusion in space and time rather than afterslip or non-linear viscous  
75 relaxation processes.

76 **Results**

77 **Surface deformation patterns**

78 The postseismic deformation model fits the observed GNSS displacement time series very well (Fig.  
79 2). Our estimated afterslip distribution locates in the region of moderate coseismic slip, which agrees  
80 with those predicted by stress-driven afterslip distributions<sup>37,38</sup>. The afterslip magnitude and location are  
81 similar to previous studies of the Iquique earthquake inverting GNSS data<sup>34,39</sup>. Still, clear differences  
82 are found near the regions of maximum afterslip, primarily because previous studies<sup>34,39</sup> have neglected  
83 poroelasticity and non-linear viscoelasticity. Afterslip dominates the horizontal component of the GNSS  
84 time-series in the near field (Fig. 2b, d, f). Nevertheless, poroelastic deformation significantly contributes  
85 to vertical surface displacements. Here, the largest poroelastic vertical surface displacements are found  
86 near the coastline, in front of the region of the largest coseismic slip release at station PSGA with an uplift  
87 of  $\sim 5$  cm. This represents about 60% of the subsidence resulting from afterslip in the near field at the  
88 stations PSGA (Fig. 2c) and IQQE (Fig. 2e). At a greater distance from the trench, non-linear viscoelastic  
89 relaxation process is the key driver of a larger fraction of the observed horizontal and most of the vertical  
90 components (see, e.g., station COLC location (Fig. 2f, g). Moreover, poroelastic processes decay faster  
91 than afterslip and non-linear viscoelastic relaxation (e.g., Fig. 2c, g).

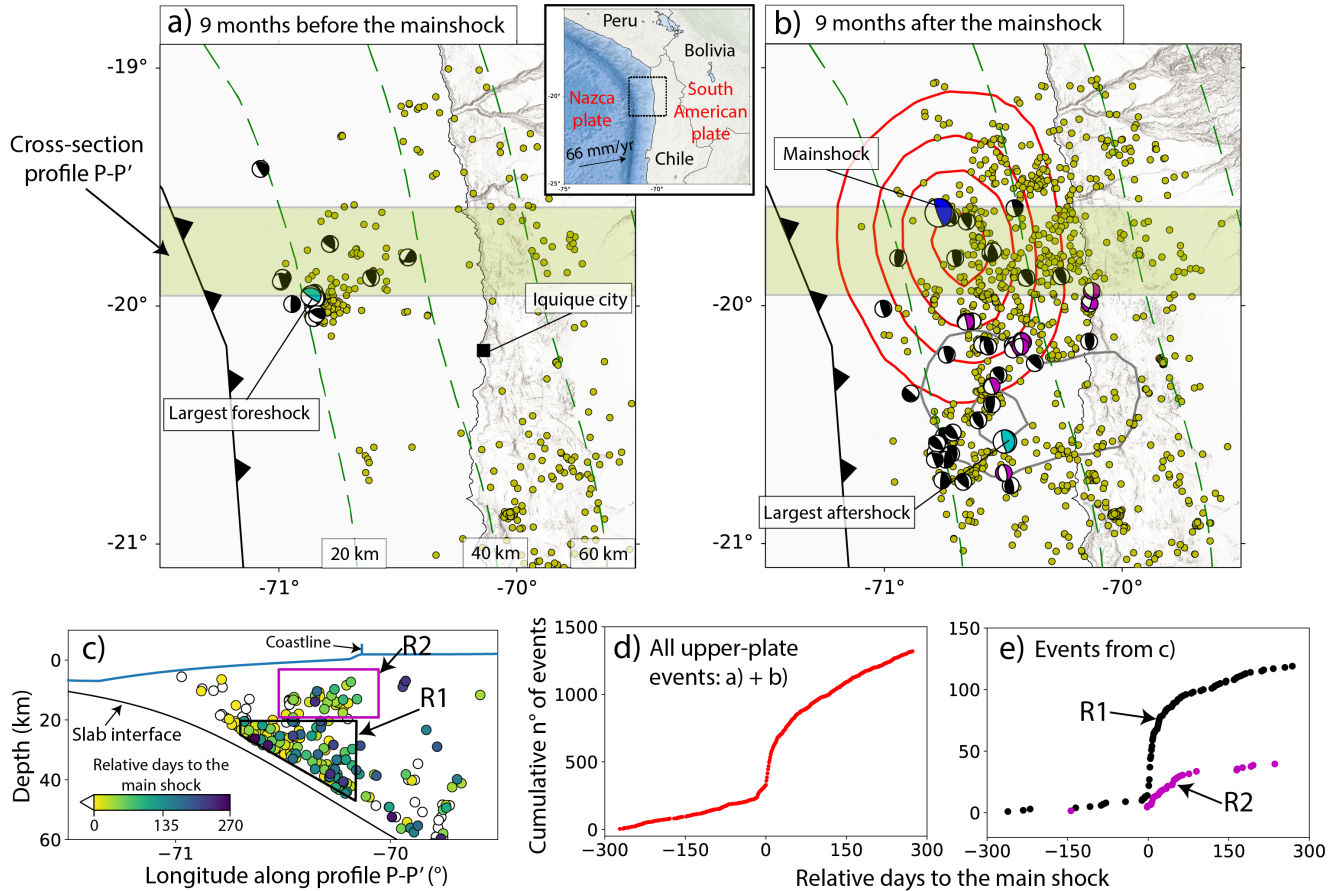


**Figure 1.** Upper-plate seismicity<sup>36</sup> in yellow circles and focal mechanisms<sup>5</sup> represented by beachballs during the nine months before (a) and nine months after (b) the mainshock. Red and grey contour lines in b) represent 1.0-m and 0.5-m of slip produced by the main shock and largest aftershock<sup>33</sup>, respectively. The plate interface is presented in green-dashed 20 km contour lines in a) and b). The cross-section P–P' is shown in c), with events color-coded by time. The cumulative number of events over time in the whole study region (a, b) is exhibited in d), and for two subregions R1 and R2 from cross-section P–P' in e).

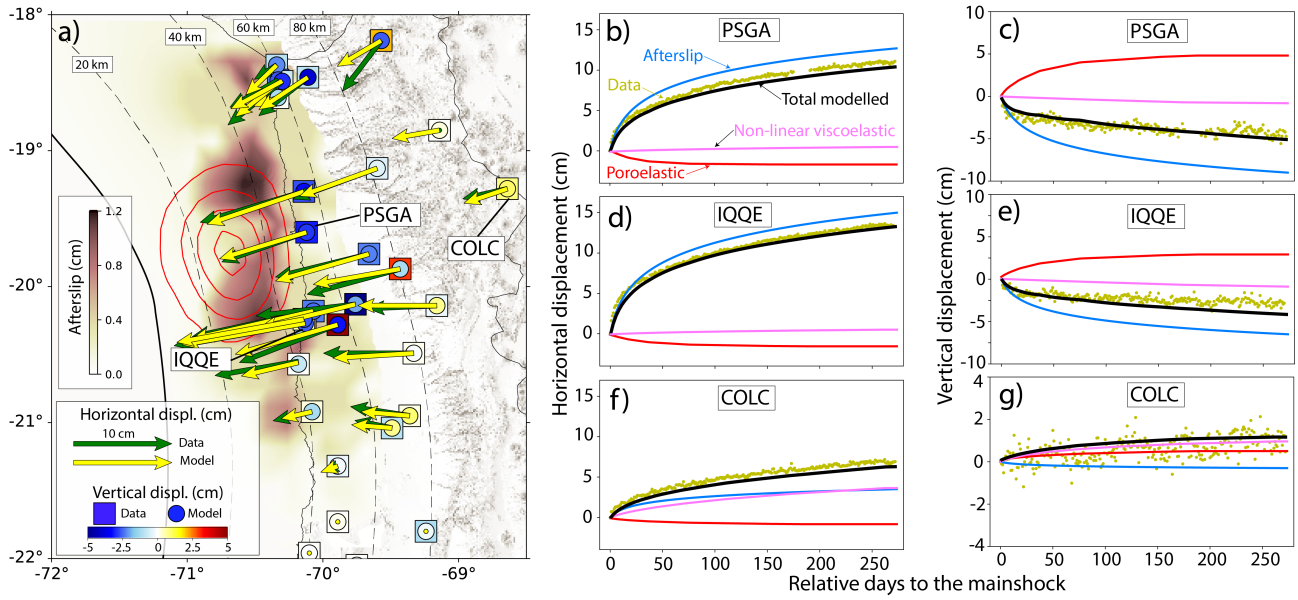


**Figure 2.** 4D observed and modelled postseismic surface deformation during the first 270 days of postseismic deformation. The cumulative sum of afterslip, poroelastic, and non-linear viscoelastic relaxation compared to the total observed surface displacements is shown in a). Background color-coded in a) depicts the inverted afterslip distribution on the fault interface considering poroelastic and non-linear viscoelastic effects projected to the surface. The relative contribution (b–g) of afterslip (in blue), poroelastic (in red), and non-linear viscoelastic relaxation (in pink) processes to the observed surface displacement time-series at stations PSGA (b, c), IQQE (d, e), and COLC (f, g).

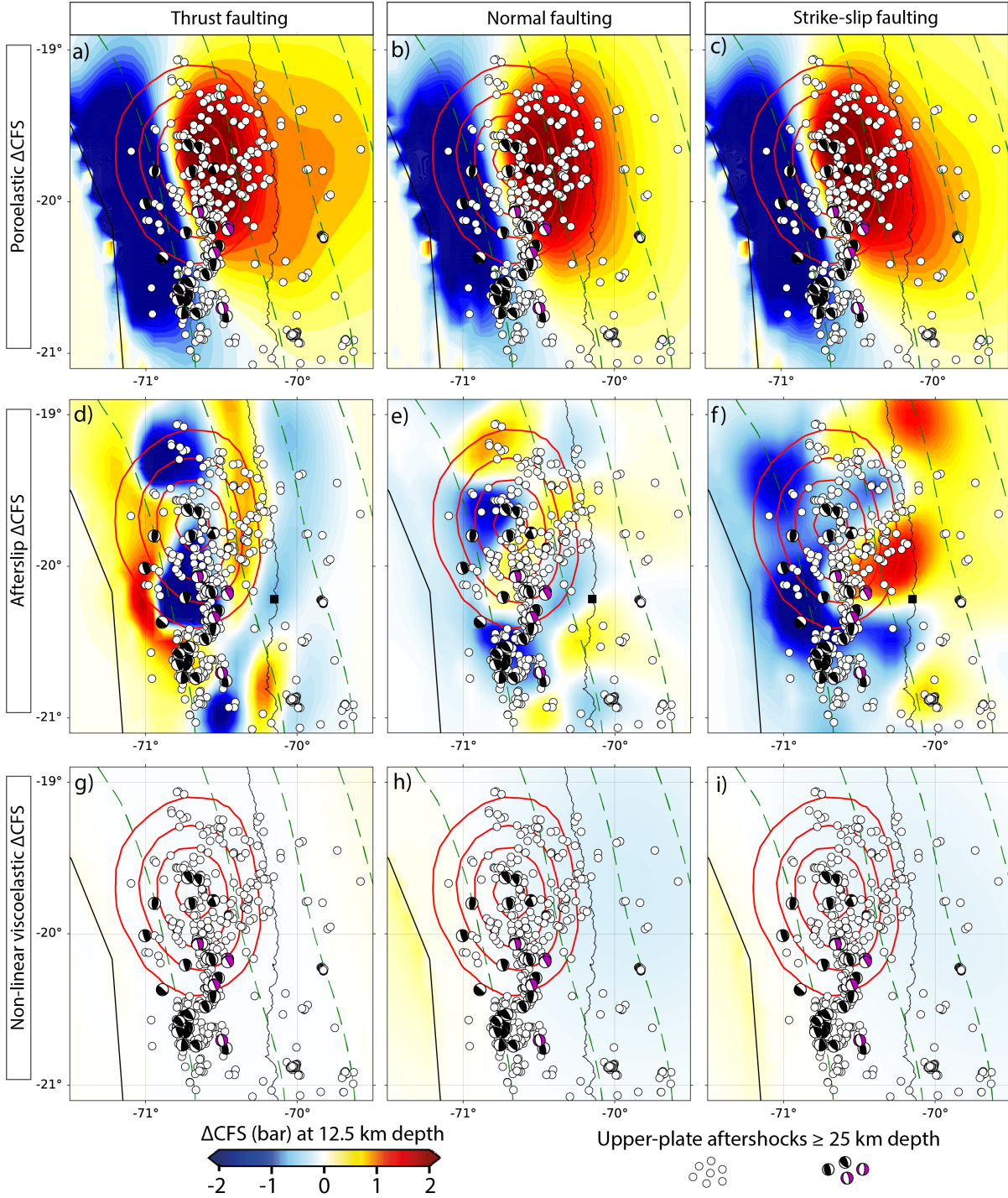


**Figure 3.** Individual cumulative  $\Delta\text{CFS}$  after 270 days at 12.5 km depth calculated from poroelastic (upper row, a–c), afterslip (middle row, d–f), and non-linear viscoelastic (lower row, g–i) processes in comparison to upper-plate aftershocks above 25 km depth. The  $\Delta\text{CFS}$  is computed for thrust and normal receiver faults, representing the two dominant faulting styles shown by earthquake focal mechanism<sup>5</sup>. Here, we average the strike, dip, and rake of the upper-plate aftershocks showing these two faulting styles. For the thrust faulting (left column), we obtain a strike, dip, and rake angle of  $137^\circ$ ,  $54^\circ$ , and  $80^\circ$ , respectively, while for the normal faulting (middle column) of  $140^\circ$ ,  $57^\circ$ , and  $104^\circ$ , respectively. For comparison, we also compute the  $\Delta\text{CFS}$  for strike-slip faulting (right column) with  $0^\circ$ ,  $90^\circ$ , and  $0^\circ$ , respectively.

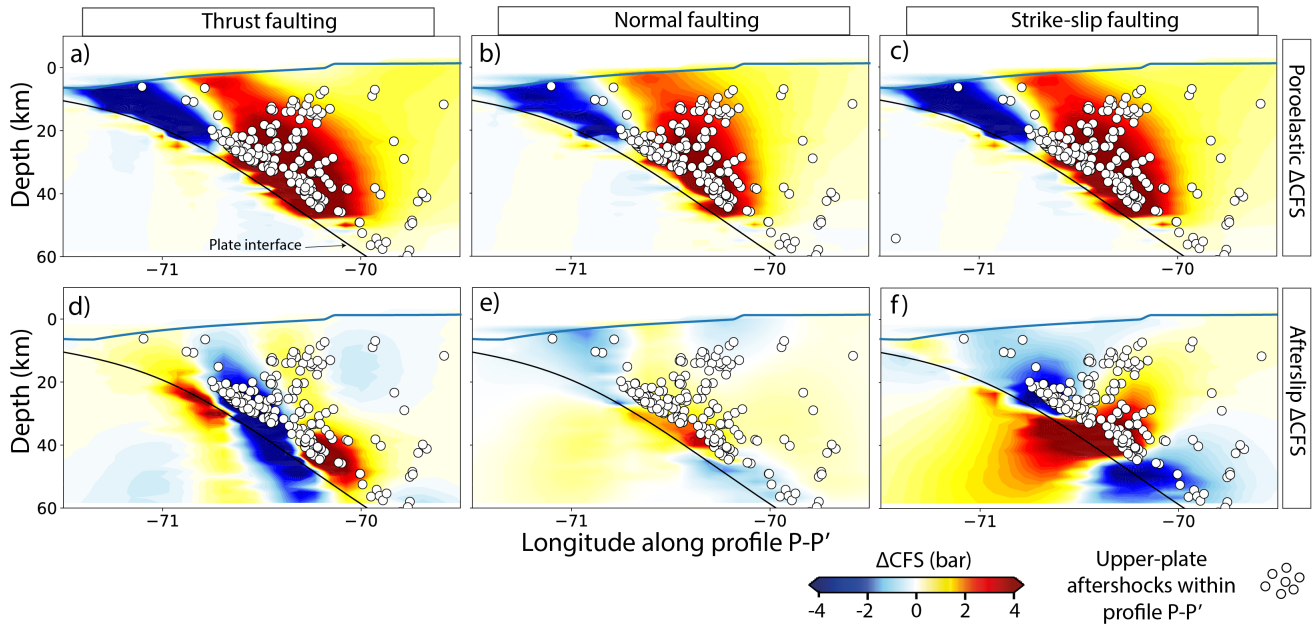


**Figure 4.** Same as Fig. 3 but along cross-section P–P' shown in Fig. 1 and for poroelastic (a–c) and afterslip (d–f) processes only.

## 92 Stress changes due to individual postseismic processes

To visualize the stress changes accumulated after 270 days resulting from each postseismic process, we estimate the value of  $\Delta\text{CFS}$  at 12.5 km depth (Fig. 3) and along the cross-section P–P' (Fig. 4). The estimation of the  $\Delta\text{CFS}$  is based on the changes of the normal and shear stress of a given fault orientation (see methods). We compute the  $\Delta\text{CFS}$  using the mean of the dominant faulting styles, i.e., steep-thrust and normal faulting, observed in the upper plate by aftershock focal mechanisms<sup>5</sup> (first and second columns, respectively, in Fig. 3 and Fig. 4). For comparison, we also estimate the  $\Delta\text{CFS}$  for a strike-slip faulting (third column in Fig. 3 and Fig. 4). The highest  $\Delta\text{CFS}$  results from pore-pressure changes in the forearc close to the coastline, with an approximate magnitude of 2.5 bar for the upper crust and 8 bar for the lower crust (Fig. 3a–c; Fig. 4a–c). In contrast to  $\Delta\text{CFS}$  produced by afterslip and viscoelastic relaxation, we find that poroelastic  $\Delta\text{CFS}$  are insensitive to the receiver fault orientation used for the  $\Delta\text{CFS}$  calculation (Fig. 3 and Fig. 4). Furthermore, the afterslip  $\Delta\text{CFS}$  values are smaller compared to those from poroelastic processes in the shallow upper plate (Fig. 3d, e, f), whereas those from non-linear viscoelastic relaxation are more than one order of magnitude lower (Fig. 3g, h, i).

## 106 Pore-pressure changes and upper-plate aftershocks occurrence in space and time

After demonstrating that  $\Delta\text{CFS}$  due to pore-pressure changes can explain the upper-plate aftershocks distribution in space much better than those from afterslip or viscoelastic relaxation, we examine if pore-pressure can also explain upper-plate aftershock temporal evolutions. The spatial and temporal distributions of postseismic pore-pressure changes and upper-plate aftershocks along the cross-section profile P–P' and in two regions of increased upper-plate aftershock activity (Fig. 1e) are exhibited in Fig.

112 5. Like the poroelastic  $\Delta$ CFS, our findings show that most upper-plate events lie in regions of increased  
 113 pore pressure (Fig. 5a). In particular, we discover a strong temporal correlation between the pore-pressure  
 114 increase and the number of upper-plate aftershocks (Fig. 5b, c). The temporal decay of upper-plate  
 115 aftershocks is a function of distance to the region of the highest coseismic slip; the aftershock region  
 116 closer to the plate interface (R1 in Fig. 5b) depicts a faster increase than the region further away (R2 in  
 117 Fig. 5c). This agrees with the temporal evolution of pore pressure since it expands from the source of  
 initial deformation, i.e., coseismic rupture, to larger distances<sup>40</sup>.

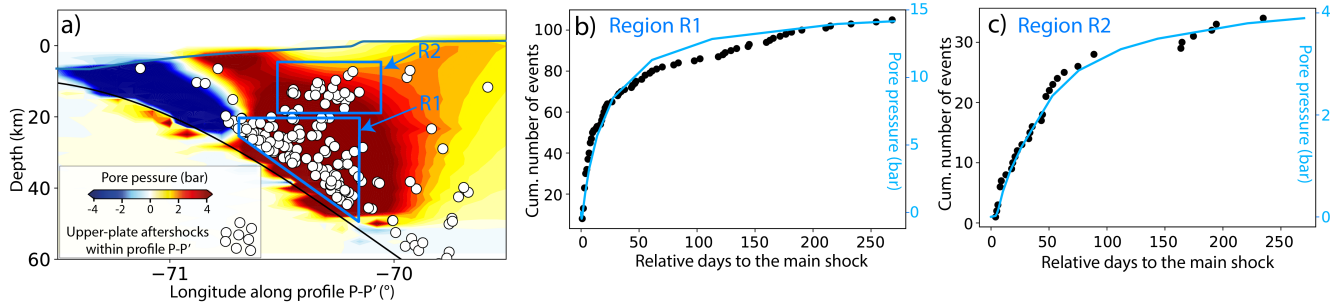


**Figure 5.** Spatial and temporal pore-pressure changes across profile P–P' (see Fig. 1a, b) and two subregions R1 and R2 after 270 days. Pore-pressure diffusion time series are computed at the center of R1 and R2.

118

## 119 Discussion

### 120 Pore-pressure diffusion in the upper plate

121 We propose that pore-pressure diffusion is the main driver of upper-plate aftershocks given its superior  
 122 correlation with spatial and especially temporal occurrence (Fig. 5), and because the poroelastic  $\Delta$ CFS  
 123 values are much larger than a critical triggering value of +0.1 bar<sup>2,7</sup> in the region where most of the upper-  
 124 plate aftershocks occur. This contrasts the widely used  $\Delta$ CFS estimation to investigate aftershock sequences  
 125 based on coseismic stress changes derived from purely elastic models in all tectonic settings<sup>2,5,7,8,41</sup>,  
 126 where stress changes are generally much smaller and which fail to explain the time-dependency. This  
 127 time dependency could be explained by the exponential decay of afterslip<sup>12,42</sup> or non-linear viscoelastic  
 128 relaxation<sup>43</sup>, but the estimation of  $\Delta$ CFS resulting from these processes is highly sensitive to the used  
 129 fault orientation and the assumed style of faulting, respectively. However, in the aftershock sequence,  
 130 we observed contrasting faulting styles that take place on closely spaced faults (Fig. 1). This pattern of  
 131 different faulting styles occurring next to each other is often observed, with examples including megathrust  
 132 events in central–south Chile<sup>3,4</sup>, northern Japan<sup>6</sup>, and the Hellenic arc (Greece)<sup>44</sup>.

133 Upper-plate aftershocks generally occur in the region of coseismic dilation (where postseismic pore  
 134 pressure increases transiently<sup>11</sup>, Fig. 5) and depict a change from thrust faulting to prevailing normal and  
 135 strike-slip faulting in the fore- and volcanic-arc regions, respectively<sup>3,6,45</sup>. Unlike fault-slip processes  
 136 (e.g., afterslip, slow slip), pore-pressure diffusion fits quite well since it acts equally in all directions of the

137 rock pore void<sup>40</sup> (Fig. 3). Therefore, increased pore pressure reduces the effective fault normal stresses  
138 independent of the fault orientation and consequently triggers all faulting styles. Our results are also  
139 supported by other studies that propose that pore-pressure changes best explain the changes in the stress  
140 field and the presence of different focal mechanisms within the subducting plate in northern Hikurangi,  
141 New Zealand<sup>26</sup>, and in the shallow crust in the transform fault zone in South Iceland<sup>23</sup>.

## 142 Crustal rock permeability in subduction zones

143 The key parameter controlling the temporal evolution of pore-pressure diffusion is rock permeability<sup>46</sup>.  
144 In our model, we used a continental crust permeability value of  $\sim 10^{14} \text{ m}^2$  as found by previous studies  
145 in northern Chile<sup>28,30</sup>, which is a relatively high permeability compared to other tectonic settings<sup>47</sup>.  
146 Nevertheless, it is about three orders of magnitude lower than in typical crustal-scale rocks found by  
147 geological field measurements in northern Chile<sup>48</sup> and similar to those obtained in other subduction zones,  
148 e.g., from the aftershock migration front following the 2004 Sumatra-Andaman earthquake, Indonesia<sup>32</sup>  
149 and hydro-mechanical-numerical modeling to explain the short-term postseismic geodetic signal in south  
150 Chile<sup>11</sup>. In addition, our calculation of diffusivity from the aftershock migration front agrees reasonably  
151 well with a permeability of  $\sim 10^{14} \text{ m}^2$  (see methods). Although we cannot neglect a transient increase in  
152 permeability due to the main shock<sup>25,47</sup>, it would increase about one order of magnitude<sup>47</sup>, which is much  
153 smaller compared to the uncertainty of permeability<sup>47</sup> and will primarily affect the amplitude but not the  
154 spatial distribution of the resulting pore-pressure changes.

## 155 Implications for time-dependent seismic hazard assessment

156 We demonstrated that pore-pressure diffusion is the key driver of aftershocks in the upper plate after  
157 the 2014 Iquique earthquake in northern Chile. The similarity of the deformation pattern imprinted in  
158 upper-plate aftershocks in other subduction zones, such as the non-linear decay over time and variable  
159 faulting styles, suggests that pore-pressure diffusion may govern the postseismic reactivation of upper-plate  
160 faults after megathrust earthquakes worldwide. This suggests the broadly used computation of static  
161  $\Delta\text{CFS}$  on optimally oriented faults to infer the potential response of upper-plate faults to megathrust earth-  
162 quakes<sup>2,49,50</sup> must be revised. In particular, faults that are not favorably oriented during the interseismic  
163 stress accumulation phase may also increase their seismic hazard potential, especially in the first weeks  
164 and months after the main shock, when pore-pressure diffusion is intense.

165 The tendency of large upper-plate aftershocks to occur close to highly-populated forearc regions<sup>2,49</sup>  
166 poses an elevated seismic risk, for instance, in cities along the subduction margins in South America, Japan,  
167 Indonesia, and Western US and Canada. Therefore, our results could be used as input for time-dependent  
168 seismic hazard assessment to estimate the first-order patterns of the distribution of pore-pressure diffusion  
169 in the upper plate based on earthquake-scenario simulations using interseismic plate-strain accumulation  
170 predicted from geodetic inversions<sup>51</sup> or forward rate-and-state friction laws modelling<sup>38</sup>.

171 **Methods**

172 **Seismicity and focal mechanisms**

173 We use a published high-resolution seismicity catalog<sup>36</sup> and a compiled earthquake focal mechanism  
174 catalog<sup>5</sup>. Sippl et al.<sup>36</sup> classified upper-plate events  $\leq 70.8^\circ\text{W}$  only, due to the deterioration of the depth  
175 accuracy further offshore. We further extend this by also including the events  $> 70.8^\circ\text{W}$  that are at a  
176 distance of more than 10 km above the plate interface<sup>52</sup>. This conservative distance estimate results from  
177 the large uncertainty of offshore events generally larger than 10-15 km for regions west of  $70.8^\circ\text{W}$  in  
178 northern Chile<sup>5,36</sup>.

179 We select the focal mechanisms in the upper plate whose rake, dip, and strike angles are off a range  
180 of  $\pm 30^\circ$  from the fault geometry of the main shock. In addition to this constraint, we also select those  
181 events whose perpendicular distance to the plate interface is larger than 10 km for  $> 70.8^\circ\text{W}$  and 4 km for  
182  $\leq 70.8^\circ\text{W}$  based on the event location uncertainty<sup>5</sup>.

183 **Continuous GNSS measurements**

184 We use published daily continuous GNSS positions from Hoffmann et al.<sup>34</sup> obtained from the IOPC net-  
185 work. The positions in the International Terrestrial Reference Frame are transformed into a regional South  
186 American Frame<sup>34</sup>. To investigate the processes that control transient postseismic deformation<sup>11,34,37</sup>, i.e.,  
187 afterslip, poroelastic and non-linear viscoelastic processes, we remove from the GNSS daily solutions the  
188 seasonals, jumps due to large aftershocks and/or antenna changes, and the interseismic linear component  
189 calculated before the 2014 main shock from positioning time-series using the trajectory model of Bevis  
190 and Brown<sup>53</sup>.

191 **Modeling strategy**

192 **Forward model**

193 We construct a 4D geomechanical-numerical model for northern Chile following the strategy of Peña et  
194 al.<sup>11</sup>. The model considers the plate interface from the Slab1.0 model<sup>52</sup>, and we set a Moho discontinuity  
195 at 50 km depth as observed by seismological studies and predicted by density models<sup>54</sup>. The model is  
196 discretized into finite elements of  $\sim 1$  km in the region of key postseismic deformation and increases up to  
197  $\sim 50$  km at the boundaries of the model. The model extent is large enough to avoid boundary artifacts. The  
198 numerical problem, i.e., frictional-fault slip, linear poroelasticity, and temperature-controlled power-law  
199 rheology (non-linear viscosity), is solved using the software ABAQUS™ version 6.14.

We implement power-law rheology with dislocation creep processes as:

$$\dot{\varepsilon} = A \sigma^n e^{\frac{-Q}{RT}} \quad (1)$$

200 Where  $\dot{\varepsilon}$  is the creep strain rate,  $A$  is a pre-exponent parameter,  $\sigma$  the differential stress,  $n$  the stress  
201 exponent,  $Q$  the activation enthalpy for creep,  $R$  the gas constant and  $T$  the absolute temperature<sup>55</sup>.  
202 We adopt the 2D temperature field of Springer<sup>56</sup> for northern Chile and extend it into our 3D model  
203 domain following Peña et al.<sup>13</sup>. We neglect linear diffusion and transient creep processes because

of the dominant role of dislocation creep processes in the lower crust and upper mantle<sup>57</sup> and high uncertainty of the temperature field at greater depths<sup>56</sup>, respectively. We use elastic and creep rock material parameters obtained from seismological studies and laboratory experiments<sup>55</sup>, respectively, while the spatial distribution of effective non-linear viscosity is driven by the temperature field. We consider for the continental crust quartzite ( $n=2.3$ ,  $A=3.2 \times 10^{-4}$  MPa $^n$  s $^{-1}$ ,  $Q=154$  kJ/mol)<sup>55</sup>, for the continental and oceanic upper mantle wet olivine with 0.1% ( $A=5.6 \times 10^{-6}$  MPa $^n$  s $^{-1}$ ) and 0.01% ( $A=1.6 \times 10^{-5}$  MPa $^n$  s $^{-1}$ ) of water content, respectively ( $n=3.5$ ,  $Q=480$  kJ/mol)<sup>55</sup>; and for the slab diabase ( $n=3.4$ ,  $A=2.0 \times 10^{-4}$  MPa $^n$  s $^{-1}$ ,  $Q=260$  kJ/mol).

Poroelasticity is implemented following the approach of Wang<sup>40</sup> that has been successfully applied in many studies<sup>11,14,46</sup>. Here, the equations of the mass conservation and Darcy's laws describe the fully-coupled displacement field ( $u$ ) and pore-fluid pressure ( $p$ ) in Cartesian coordinates ( $x$ ) expressed in index notation as follows:

$$G\nabla^2 u_i + \frac{G}{(1-2v)} \frac{\partial^2 u_k}{\partial x_i \partial x_k} = \alpha \frac{\partial p}{\partial x_i} \quad (2)$$

$$\alpha \frac{\partial \varepsilon_{kk}}{\partial t} + S_\varepsilon \frac{\partial p}{\partial t} = \frac{\kappa}{u_f} \nabla^2 p \quad (3)$$

Where  $v$  and  $G$  correspond to the drained Poisson ratio and shear modulus, respectively,  $t$  the elapsed time since the main shock,  $\alpha$  the Biot-Willis coefficient,  $S_\varepsilon$  the constrained storage coefficient,  $\varepsilon_{kk} = \frac{\partial u_k}{\partial x_k}$  the volumetric strain,  $\kappa$  the intrinsic rock permeability, and  $u_f$  the pore-fluid viscosity. The subscript  $i$  denotes the three orthogonal spatial directions, while the subscript  $k$  is the summation over these three components<sup>14</sup>.

We also obtain the upper-plate permeability indirectly from the aftershock migration front. The relation of diffusivity and permeability are related as  $\kappa = D\phi\mu/K_f$  where  $\kappa$  corresponds to the permeability,  $D$  is the diffusivity,  $\phi$  the rock porosity,  $\mu$  the dynamic viscosity, and  $K_f$  the pore fluid (water) bulk modulus<sup>40</sup>.  $D$  is obtained from the aftershock migration using  $r = \sqrt{4\pi Dt_{elap}}$  with  $r$  the hypocenter distance to the main shock and  $t_{elap}$  the elapsed time since the main shock. Our regression gives a value of  $D=60$  m $^2$ /s and using crustal scale rock parameters of  $K_f=2.3$  GPa<sup>13,40,46</sup>,  $\phi=0.005$ <sup>30,40</sup>, and  $\mu=10^{-4}$  Pa s<sup>30</sup>, we obtain a permeability value of  $1.3 \times 10^{-14}$  m $^2$ .

### **Inversion approach and stress and pore-pressure changes**

We use an inversion approach to obtain the cumulative afterslip distribution up to the end of 2015, i.e., over ca. nine months. We first calculate the cumulative poroelastic and non-linear viscoelastic components at the GNSS sites by running a forward simulation. Then, we remove these poroelastic and viscoelastic components from the GNSS measurements and use a linear inversion approach with Laplacian constraints that minimizes the residual GNSS data<sup>11,13</sup>. The temporal distribution of the afterslip is calculated following a well-established time-dependent function from stress-driven afterslip studies as

235  $A(t) = A_0 \log \frac{t_a + t_c}{t_r}$  with  $A_0$  as the amplitude obtained from the inversion,  $t_a$  is the elapsed time after the  
236 main shock,  $t_r$  is the characteristic time of relaxation, and  $t_c$  the critical time, which is introduced to avoid  
237 the singularity at  $t = 0$ <sup>11, 16</sup>.

The Coulomb Failure Stress changes ( $\Delta CFS$ ) from each postseismic process are calculated as:

$$\Delta CFS = \Delta\tau - \mu_{fr}\Delta(\sigma - P) \quad (4)$$

238 Here,  $\tau$  is the shear stress,  $\mu_{fr}$  is the coefficient of friction,  $\sigma$  is the normal stress, and  $P$  is the pore  
239 pressure. We consider a  $\mu_{fr}=0.6$ <sup>2, 7, 8</sup>, while  $\tau$ ,  $\sigma$ , and  $P$  are directly obtained from the model outputs. The  
240  $\Delta CFS$  are computed on Tecplot 360 EX<sup>58, 59</sup>. For the afterslip and non-linear viscoelastic calculations, we  
241 consider  $P=0$  MPa since it is then calculated separately as the poroelastic contribution.

## 242 References

- 243 1. Omori, F. *On the after-shocks of earthquakes*. Ph.D. thesis, The University of Tokyo (1895).
- 244 2. Toda, S., Stein, R. S. & Lin, J. Widespread seismicity excitation throughout central Japan following  
245 the 2011 M= 9.0 Tohoku earthquake and its interpretation by coulomb stress transfer. *Geophys. Res.  
246 Lett.* **38**, DOI: <https://doi.org/10.1029/2011GL047834> (2011).
- 247 3. Lupi, M. & Miller, S. A. Short-lived tectonic switch mechanism for long-term pulses of volcanic  
248 activity after mega-thrust earthquakes. *Solid Earth* **5**, 13–24, DOI: [10.5194/se-5-13-2014](https://doi.org/10.5194/se-5-13-2014) (2014).
- 249 4. Lange, D. *et al.* Aftershock seismicity of the 27 February 2010 Mw 8.8 Maule earthquake rupture  
250 zone. *Earth Planet. Sci. Lett.* **317**, 413–425, DOI: <https://doi.org/10.1016/j.epsl.2011.11.034> (2012).
- 251 5. Soto, H. *et al.* Probing the Northern Chile megathrust with seismicity: The 2014 M8.1 Iquique  
252 earthquake sequence. *J. Geophys. Res. Solid Earth* **124**, 12935–12954a, DOI: [https://doi.org/10.1029/2019JB017794](https://doi.org/10.1029/253) (2019).
- 254 6. Nakamura, W., Uchida, N. & Matsuzawa, T. Spatial distribution of the faulting types of small  
255 earthquakes around the 2011 Tohoku-oki earthquake: A comprehensive search using template events.  
256 *J. Geophys. Res. Solid Earth* **121**, 2591–2607, DOI: <https://doi.org/10.1002/2015JB012584> (2016).
- 257 7. Freed, A. M. Earthquake triggering by static, dynamic, and postseismic stress transfer. *Annu. Rev.  
258 Earth Planet. Sci.* **33**, 335–367, DOI: <https://doi.org/10.1146/annurev.earth.33.092203.122505> (2005).
- 259 8. Jara-Muñoz, J., Melnick, D. & Li, S. e. a. The cryptic seismic potential of the Pichilemu blind fault in  
260 Chile revealed by off-fault geomorphology. *Nat Commun* DOI: [10.1038/s41467-022-30754-1](https://doi.org/10.1038/s41467-022-30754-1) (2022).
- 261 9. Wang, K. *et al.* Stable forearc stressed by a weak megathrust: Mechanical and geodynamic implica-  
262 tions of stress changes caused by the M= 9 Tohoku-oki earthquake. *J. Geophys. Res. Solid Earth* **124**,  
263 6179–6194, DOI: <https://doi.org/10.1029/2018JB017043> (2019).
- 264 10. Dielforder, A. *et al.* Megathrust stress drop as trigger of aftershock seismicity: Insights from the 2011  
265 Tohoku earthquake, Japan. *Geophys. Res. Lett.* **50**, e2022GL101320, DOI: [https://doi.org/10.1029/2022GL101320](https://doi.org/10.1029/266) (2023).

- 267 11. Peña, C. *et al.* Role of Poroelasticity During the Early Postseismic Deformation of the 2010 Maule  
268 Megathrust Earthquake. *Geophys. Res. Lett.* **49**, e2022GL098144, DOI: <https://doi.org/10.1029/2022GL098144> (2022).
- 270 12. Cattania, C., Hainzl, S., Wang, L., Enescu, B. & Roth, F. Aftershock triggering by postseismic stresses:  
271 A study based on Coulomb rate-and-state models. *J. Geophys. Res. Solid Earth* **120**, 2388–2407, DOI:  
272 <https://doi.org/10.1002/2014JB011500> (2015).
- 273 13. Peña, C. *et al.* Impact of power-law rheology on the viscoelastic relaxation pattern and afterslip  
274 distribution following the 2010 Mw 8.8 Maule earthquake. *Earth Planet. Sci. Lett.* **542**, 116292, DOI:  
275 <https://doi.org/10.1016/j.epsl.2020.116292> (2020).
- 276 14. Hughes, K. L., Masterlark, T. & Mooney, W. D. Poroelastic stress-triggering of the 2005 M8.7 Nias  
277 earthquake by the 2004 M9.2 Sumatra–Andaman earthquake. *Earth Planet. Sci. Lett.* **293**, 289–299,  
278 DOI: <https://doi.org/10.1016/j.epsl.2010.02.043> (2010).
- 279 15. Wang, K., Hu, Y. & He, J. Deformation cycles of subduction earthquakes in a viscoelastic Earth.  
280 *Nature* **484**, 327, DOI: <https://doi.org/10.1038/nature11032> (2012).
- 281 16. Avouac, J.-P. From geodetic imaging of seismic and aseismic fault slip to dynamic modeling of the  
282 seismic cycle. *Annu. Rev. Earth Planet. Sci.* **43**, 233–271 (2015).
- 283 17. Weiss, J. R. *et al.* Illuminating subduction zone rheological properties in the wake of a giant earthquake.  
284 *Sci. advances* **5**, eaax6720, DOI: [10.1126/sciadv.aax6720](https://doi.org/10.1126/sciadv.aax6720) (2019).
- 285 18. McCormack, K. A. & Hesse, M. A. Modeling the poroelastic response to megathrust earthquakes:  
286 A look at the 2012 Mw 7.6 Costa Rican event. *Adv. Water Resour.* **114**, 236–248, DOI: <https://doi.org/10.1016/j.advwatres.2018.02.014> (2018).
- 288 19. Nur, A. & Booker, J. R. Aftershocks caused by pore fluid flow? *Sci. (New York, N.Y.)* **175**, 885–7,  
289 DOI: [10.1126/science.175.4024.885](https://doi.org/10.1126/science.175.4024.885) (1972).
- 290 20. Ellsworth, W. L. Injection-induced earthquakes. *science* **341**, 1225942, DOI: [10.1126/science.1225942](https://doi.org/10.1126/science.1225942)  
291 (2013).
- 292 21. Yu, H., Harrington, R. M., Kao, H., Liu, Y. & Wang, B. Fluid-injection-induced earthquakes  
293 characterized by hybrid-frequency waveforms manifest the transition from aseismic to seismic slip.  
294 *Nat. Commun.* **12**, 1–11, DOI: <https://doi.org/10.1038/s41467-021-26961-x> (2021).
- 295 22. Goebel, T., Weingarten, M., Chen, X., Haffener, J. & Brodsky, E. The 2016 Mw5. 1 Fairview,  
296 Oklahoma earthquakes: Evidence for long-range poroelastic triggering at > 40 km from fluid disposal  
297 wells. *Earth Planet. Sci. Lett.* **472**, 50–61, DOI: <https://doi.org/10.1016/j.epsl.2017.05.011> (2017).
- 298 23. Geoffroy, L. *et al.* Hydrothermal fluid flow triggered by an earthquake in Iceland. *Commun. Earth &*  
299 *Environ.* **3**, 1–9, DOI: <https://doi.org/10.1038/s43247-022-00382-0> (2022).
- 300 24. Miller, S. A. *et al.* Aftershocks driven by a high-pressure CO<sub>2</sub> source at depth. *Nature* **427**, 724–7,  
301 DOI: <https://doi.org/10.1038/nature02251> (2004).

- 302 25. Miller, S. A. Aftershocks are fluid-driven and decay rates controlled by permeability dynamics. *Nat. communications* **11**, 5787, DOI: <https://doi.org/10.1038/s41467-020-19590-3> (2020).
- 303
- 304 26. Warren-Smith, E. *et al.* Episodic stress and fluid pressure cycling in subducting oceanic crust during  
305 slow slip. *Nat. Geosci.* **12**, 475–481, DOI: <https://doi.org/10.1038/s41561-019-0367-x> (2019).
- 306 27. Peacock, S. A. Fluid processes in subduction zones. *Science* **248**, 329–337, DOI: [10.1126/science.248.4953.329](https://doi.org/10.1126/science.248.4953.329) (1990).
- 307
- 308 28. Koerner, A., Kissling, E. & Miller, S. A. A model of deep crustal fluid flow following the Mw =  
309 8.0 Antofagasta, Chile, earthquake. *J. Geophys. Res. Solid Earth* **109**, DOI: <https://doi.org/10.1029/2003JB002816> (2004).
- 310
- 311 29. Husen, S. & Kissling, E. Postseismic fluid flow after the large subduction earthquake of Antofagasta,  
312 Chile. *Geology* **29**, 847–850, DOI: [https://doi.org/10.1130/0091-7613\(2001\)029<0847:PFFATL>2.0.CO;2](https://doi.org/10.1130/0091-7613(2001)029<0847:PFFATL>2.0.CO;2) (2001).
- 313
- 314 30. Shapiro, S., Patzig, R., Rothert, E. & Rindschwentner, J. Triggering of seismicity by pore-pressure  
315 perturbations: Permeability-related signatures of the phenomenon. *Pure Appl. Geophys.* 1051–1066,  
316 DOI: [0033-4553/03/061051-16](https://doi.org/10.1007/s00160-003-4553-0) (2003).
- 317
- 318 31. Amezawa, Y., Maeda, T. & Kosuga, M. Migration diffusivity as a controlling factor in the duration of  
319 earthquake swarms. *Earth, Planets Space* **73**, 1–11, DOI: <https://doi.org/10.1186/s40623-021-01480-7> (2021).
- 320
- 321 32. Waldhauser, F., Schaff, D. P., Diehl, T. & Engdahl, E. R. Splay faults imaged by fluid-driven  
322 aftershocks of the 2004 Mw 9.2 Sumatra-Andaman earthquake. *Geology* **40**, 243–246, DOI: <https://doi.org/10.1130/G32420.1> (2012).
- 323
- 324 33. Schurr, B. *et al.* Gradual unlocking of plate boundary controlled initiation of the 2014 Iquique  
325 earthquake. *Nature* **512**, 299–302, DOI: <https://doi.org/10.1038/nature13681> (2014).
- 326
- 327 34. Hoffmann, F. *et al.* Characterizing afterslip and ground displacement rate increase following the 2014  
328 Iquique-Pisagua Mw 8.1 earthquake, Northern Chile. *J. Geophys. Res. Solid Earth* **123**, 4171–4192,  
329 DOI: <https://doi.org/10.1002/2017JB014970> (2018).
- 329
- 330 35. Socquet, A. *et al.* An 8 month slow slip event triggers progressive nucleation of the 2014 Chile  
331 megathrust. *Geophys. Res. Lett.* **44**, 4046–4053, DOI: <https://doi.org/10.1002/2017GL073023> (2017).
- 332
- 333 36. Sippl, C., Schurr, B., Asch, G. & Kummerow, J. Seismicity structure of the Northern Chile forearc  
334 from >100,000 double-difference relocated hypocenters. *J. Geophys. Res. Solid Earth* **123**, 4063–4087,  
335 DOI: <https://doi.org/10.1002/2017JB015384> (2018).
- 335
- 336 37. Agata, R. *et al.* Rapid mantle flow with power-law creep explains deformation after the 2011 Tohoku  
337 mega-quake. *Nat. communications* **10**, 1–11, DOI: <https://doi.org/10.1038/s41467-019-08984-7>  
338 (2019).
- 338

- 336 38. Barbot, S. Frictional and structural controls of seismic super-cycles at the Japan trench. *Earth, Planets*  
337 *Space* **72**, 1–25, DOI: <https://doi.org/10.1186/s40623-020-01185-3> (2020).
- 338 39. Shrivastava, M. N. *et al.* Earthquake segmentation in northern Chile correlates with curved plate  
339 geometry. *Sci. reports* **9**, 1–10, DOI: <https://doi.org/10.1038/s41598-019-40282-6> (2019).
- 340 40. Wang, H. *Theory of linear poroelasticity with applications to geomechanics and hydrogeology*, vol. 2  
341 (Princeton university press, 2000).
- 342 41. Bloch, W. *et al.* The 2015–2017 Pamir earthquake sequence: foreshocks, main shocks and aftershocks,  
343 seismotectonics, fault interaction and fluid processes. *Geophys. J. Int.* **233**, 641–662, DOI: <https://doi.org/10.1093/gji/ggac473> (2023).
- 344 42. Perfettini, H., Frank, W., Marsan, D. & Bouchon, M. Updip and along-strike aftershock migration  
345 model driven by afterslip: Application to the 2011 Tohoku-Oki aftershock sequence. *J. Geophys. Res.  
346 Solid Earth* **124**, 2653–2669, DOI: <https://doi.org/10.1029/2018JB016490> (2019).
- 347 43. Zhang, X. & Shcherbakov, R. Power-law rheology controls aftershock triggering and decay. *Sci.  
348 reports* **6**, 1–9, DOI: <https://doi.org/10.1038/srep36668> (2016).
- 349 44. Mouslopoulou, V. *et al.* Earthquake Swarms, Slow Slip and Fault Interactions at the Western-End  
350 of the Hellenic Subduction System Precede the Mw 6.9 Zakynthos Earthquake, Greece. *Geochem.  
351 Geophys. Geosystems* **21**, e2020GC009243, DOI: <https://doi.org/10.1029/2020GC009243> (2020).
- 352 45. Sibson, R. H. Stress switching in subduction forearcs: Implications for overpressure containment and  
353 strength cycling on megathrusts. *Tectonophysics* **600**, 142–152, DOI: [https://doi.org/10.1016/j.tecto.2013.02.035](https://doi.org/10.1016/j.tecto.<br/>354 2013.02.035) (2013).
- 355 46. Tung, S. & Masterlark, T. Delayed poroelastic triggering of the 2016 October Visso earthquake by  
356 the August Amatrice earthquake, Italy. *Geophys. Res. Lett.* **45**, 2221–2229, DOI: [https://doi.org/10.1002/2017GL076453](https://doi.org/10.<br/>357 1002/2017GL076453) (2018).
- 358 47. Manga, M. *et al.* Changes in permeability caused by transient stresses: Field observations, experiments,  
359 and mechanisms. *Rev. Geophys.* **50**, DOI: <https://doi.org/10.1029/2011RG000382> (2012).
- 360 48. Gomila, R. *et al.* Palaeopermeability anisotropy and geometrical properties of sealed-microfractures  
361 from micro-CT analyses: An open-source implementation. *Micron* **117**, 29–39, DOI: [https://doi.org/10.1016/j.micron.2018.11.001](https://doi.org/<br/>362 10.1016/j.micron.2018.11.001) (2019).
- 363 49. Melnick, D. *et al.* Hidden Holocene slip along the coastal El Yolki fault in central Chile and its  
364 possible link with megathrust earthquakes. *J. Geophys. Res. Solid Earth* **124**, 7280–7302, DOI:  
365 <https://doi.org/10.1029/2018JB017188> (2019).
- 366 50. Terakawa, T., Hashimoto, C. & Matsu’ura, M. Changes in seismic activity following the 2011  
367 Tohoku-oki earthquake: effects of pore fluid pressure. *Earth Planet. Sci. Lett.* **365**, 17–24, DOI:  
368 <https://doi.org/10.1016/j.epsl.2013.01.017> (2013).
- 369

- 370 51. Moreno, M., Rosenau, M. & Oncken, O. 2010 Maule earthquake slip correlates with pre-seismic  
371 locking of Andean subduction zone. *Nature* **467**, 198–202, DOI: <https://doi.org/10.1038/nature09349>  
372 (2010).
- 373 52. Hayes, G. P., Wald, D. J. & Johnson, R. L. Slab1. 0: A three-dimensional model of global subduction  
374 zone geometries. *J. Geophys. Res. Solid Earth* **117**, DOI: <https://doi.org/10.1029/2011JB008524>  
375 (2012).
- 376 53. Bevis, M. & Brown, A. Trajectory models and reference frames for crustal motion geodesy. *J. Geod.*  
377 **88**, 283–311, DOI: <https://doi.org/10.1007/s00190-013-0685-5> (2014).
- 378 54. Tassara, A. & Echaurren, A. Anatomy of the Andean subduction zone: three-dimensional density  
379 model upgraded and compared against global-scale models. *Geophys. J. Int.* **189**, 161–168, DOI:  
380 <https://doi.org/10.1111/j.1365-246X.2012.05397.x> (2012).
- 381 55. Hirth, G. & Kohlstedf, D. Rheology of the upper mantle and the mantle wedge: A view from  
382 the experimentalists. *Geophys. monograph-american geophysical union* **138**, 83–106, DOI: <https://doi.org/10.1029/138GM06> (2003).
- 384 56. Springer, M. Interpretation of heat-flow density in the Central Andes. *Tectonophysics* **306**, 377–395,  
385 DOI: [https://doi.org/10.1016/S0040-1951\(99\)00067-0](https://doi.org/10.1016/S0040-1951(99)00067-0) (1999).
- 386 57. Peña, C. *et al.* Role of Lower Crust in the Postseismic Deformation of the 2010 Maule  
387 Earthquake: Insights from a Model with Power-Law Rheology. *Pure Appl. Geophys.* DOI:  
388 [10.1007/s00024-018-02090-3](https://doi.org/10.1007/s00024-018-02090-3) (2019).
- 389 58. Peña, C., Heidbach, O., Moreno, M., Melnick, D. & Oncken, O. Transient deformation and stress  
390 patterns induced by the 2010 Maule earthquake in the Illapel segment. *Front. Earth Sci.* **9**, 644834,  
391 DOI: <https://doi.org/10.1002/2016GL071845> (2021).
- 392 59. Heidbach, O., Ziegler, M. & Stromeyer, D. Manual of the tecplot 360 add-on geostress v2. 0. DOI:  
393 <https://doi.org/10.2312/wsm.2020.001> (2020).

394 **Acknowledgements**

395 This work was supported by the project Present-day Kinematics of the Southern and Eastern Alps  
396 (ALPSHAPE), funded by the DFG, Germany, 442567237 (S. M., C. P.) and the Postdoc-Bridge program,  
397 postdoctoral scholarship, funded by the University of Potsdam, Germany (C. P.).

398 **Author contributions statement**

399 C. P. conceived the original idea, elaborated with O. H. and B. S. C. P. and M. M. constructed the finite-  
400 element model. C. P. conducted all numerical simulations and the geodetic afterslip inversion. C. P. and  
401 O. H. performed the analysis of stress and pore-pressure changes. C. P., M. M., and S. M. performed the  
402 GNSS time-series analysis. O. H., O. O., and C. F. provided knowledge about structural geology and

<sup>403</sup> pore-pressure diffusion processes. C. P. and B. S. compiled and analyzed seismicity and focal mechanisms.  
<sup>404</sup> O. H., S. M., and C. F. provided the funding to carry out the research. C. P. wrote the manuscript with  
<sup>405</sup> comments from all authors.

<sup>406</sup> **Competing interests**

<sup>407</sup> The authors declare no competing interests.

<sup>408</sup> **Additional information**

<sup>409</sup> **Correspondence and requests for materials** should be addressed to C. P.